Interfacial Phenomena during Salt Layer Formation under High Rate Dissolution Conditions

Joshua A. Hammons,[†] Alison J. Davenport,[‡] S. Majid Ghahari,[‡] Mehdi Monir,[‡] Jean-Phillipe Tinnes,[†] Mahrez Amri,[†] Nick Terrill,[§] Federica Marone,[∥] Rajmund Mokso,[∥] Marco Stampanoni,[∥] and Trevor Rayment*,[§]

[†]School of Chemistry, University of Birmingham, B15 2TT, Birmingham, United Kingdom

[‡]School of Metallurgy and Materials, University of Birmingham, B15 2TT, United Kingdom

[§]Diamond Light Source Ltd., Diamond House, Harwell Science and Innovation Campus, Didcot, Oxfordshire OX11 0DE, United Kingdom

[∥]Swiss Light Source, Paul Scherrer Institute, CH-5232 Villigen, Switzerland

Ⓢ Supporting Information

ABSTRACT: Interfacial phenomena occurring during high metal dissolution rates, in an environment with diffusion-limited transport of dissolution products, have been investigated using time-resolved X-ray diffraction (XRD), small-angle X-ray scattering (SAXS) and fast radiography. Time resolved SAXS data reveal that highly anisotropic interfacial X-ray scattering always precedes salt nucleation. The correlation between the interfacial scattering the presence of salt crystals indicates that the interface is between the metal electrode and the concentrated $NiCl_2$ electrolyte and can therefore be interpreted as reflectivity or Porod scattering. Using fast radiography, we show that continued crystal nucleation and growth results in formation of a crystal-containing salt layer, which initially extends far from the interface (>20 μm), until the $NiCl_2$ concentration decreases below saturation. Dissolution of this thick salt layer occurs mainly at the furthest boundary from the interface until, the salt layer thickness decreases to a steady state value, resulting in a steady state limiting current. These results show that the presence of a crystalline salt layer at a dissolving interface causes microscopic roughening which has implications for understanding both the role of salt films in pitting corrosion and electrochemical processing.
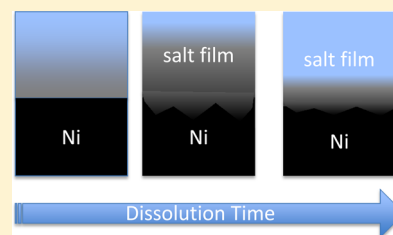
INTRODUCTION

This study focuses on interfacial phenomena that occur during rapid metal dissolution under diffusion-limited conditions. To achieve this, nickel is used as the metal of choice because it is a single component metal, has a relatively high density, and is also commonly used. Metals can dissolve at high rates during electrochemically driven processes such as electropolishing and electrochemical machining, and in forms of localized corrosion such as pitting, in which cavities propagate under metal surfaces. Electrochemical dissolution of metal is an autocatalytic process, since the resulting local high concentration of metal ions next to the surface forms a highly acidic solution (through hydrolysis reactions) and presence of a high concentration of anions, both of which further increases the rate of dissolution.[1] However, in circumstances where transport becomes diffusion-limited (which is the case with occluded cavities formed during pitting corrosion), the solution adjacent to the dissolving interface becomes supersaturated, and a granular solid salt layer[2] precipitates. This layer can substantially decrease the rate of dissolution since current is carried through the salt layer only via electrolyte present in between salt crystals. Thus the composition and the porosity of the film will strongly influence electropolishing and corrosion rates. Furthermore, salt films also play a significant role in the stability of corrosion pits by providing a "reservoir" of metal ions that can maintain an aggressive acidic solution chemistry near the interface even in the presence of a high rate of ion transport out of pits, for example after the rupture of a protective lacy cover over a corrosion pit.[3] Subsequent growth of the pit may then be controlled by ion transport through the salt film.[4] "Brightening" and "leveling" which are important properties of electro-polished and electromachined processes are known to be controlled by the presence of a salt film.[5]

In the presence of a salt layer, the current density is independent of increasing applied potential since the rate of transport of metal ions away from the dissolving interface is diffusion limited.[6] It has been proposed that in such situations for iron[4,7] and nickel[4,8−10] increases in potential lead to an increase in potential drop solely across the salt layer which in turn implies an increase in layer thickness. The principal assumption in this hypothesis[6,7] is that no concentration gradient exists inside the film, as the concentration is considered to be at saturation; most often, it is assumed that there is a bulk salt layer that is uniformly composed of salt and

saturated metal chloride solution,[4,8−12] There is no published experimental evidence to support these assumptions, and the effect of changing concentrations upon chemical speciation and concomitant changes in transport properties have largely been neglected.

While there has been some work involving transport modeling to predict concentration gradients inside the film,[13] but these are difficult to experimentally verify. The application of transport theories[14] that neglect short-range interactions[15] and other concentration affects[16,17] have successfully explained many phenomena of pitting in both artificial pits[3,18] and real pits.[12] However, electrochemical impedance spectroscopy measurements on artificial pits have deduced a capacitive component near the interface.[7,10] This was explained as a nonporous layer that exists between the dissolving metal and salt film.[7,10]

However, to our knowledge there has been no theoretical proof of how such a layer can form during dissolution and there has been no work to characterize the supersaturated solutions adjacent to dissolving interfaces from which salt films precipitate. Owing to the difficulty of carrying out in situ measurements on rapidly dissolving surfaces there has been very little work on their structural and chemical characterization apart from two studies using X-ray diffraction[9] and Raman spectroscopy.[10] The motivation of this study is to provide experimental data which can be used for future transport[10] modeling in systems such as pitting corrosion, electropolishing, and electromachining where high dissolution rates occur in highly concentrated solutions.

Time resolved X-ray diffraction (XRD) and small-angle X-ray scattering (SAXS) are used here to observe crystalline phases and any phases at the interface, respectively. A scattering phase is typically on the nanometer scale for X-rays and has an electron density different than that of its surrounding matrix.[19] Details of the SAXS methodology and theory are discussed in the Results and Analysis section.

EXPERIMENTAL SECTION

Artificial pits" are metal foils or wires embedded in an inert mount are commonly used to simulate pit propagation because they provide a 1-D diffusion path for which transport is restricted. The cross section of the embedded foil or wire is exposed and the metal is dissolved until there is a cavity that is sufficiently deep that 1-D diffusion and resistance down the cavity dominate over their effect at the pit mouth. Artificial pit studies on nickel electrodes dissolving in solutions of HCl have previously established that once the rate of dissolution of the metal exceeds the transport of metal ions to the pit mouth, then the solution becomes supersaturated, and subsequently produces a salt film[8] of $NiCl_2(H_2O)_6$.[9,10] An artificial pit was constructed as previously reported;[9] a 50 μm nickel foil (Aldrich) was embedded in epoxy resin (Araldite) and attached with Kapton tape to a simple PVC electrochemical cell which contained a Ag/AgCl reference electrode a platinum wire counter electrode in 1 M HCl. All experiments were performed at room temperature, ca. 20 °C, and potentials are quoted on the Ag/AgCl scale. Nickel foils were dissolved to pit depths of between 1 mm to 2 mm at a potential of ca. 0.9 V prior to collecting X-ray data, thereby providing a horizontal approximately linear electrode, sandwiched between kapton windows for investigation study by X-rays. The kinetics of salt layer formation was studied by the application of a positive potentiostatic step to a value sufficient to ensure the presence

of a salt layer. The target potential ranged from 1.4 to 1.8 V and system potential was held at 0 V for a period of 5 min prior to the potentiostatic step to ensure that there was no salt film was present before collecting X-ray data.

Time Resolved Small Angle X-ray Scattering (SAXS) and X-ray Diffraction XRD. Small Angle X-ray Scattering (SAXS) and X-ray Diffraction (XRD) experiments were performed at Diamond Light Source on Beamline I22 with a beam size of 70 μm (v) by 320 μm (h) at an energy of 10 keV and a q range of 0.006 Å^{-1}> q > 0.2 Å^{-1}. The position of the sample was maintained such that the interfacial region of the system was within the X-ray beam (see Appendix A, Supporting Information, SI, for further details). The XRD data were collected using a 1-D gas micro strip HOTWAXS detector simultaneously with a 2-D photon counting gas wire detector, using the RAPID system.[20] Ten second exposure times were used to obtain a suitable 2-D SAXS/1-D XRD patterns, which were calibrated using wet rat-tail collagen and NBS silicon, respectively. Electrochemical data were synchronized with the SAXS/WAXS data by recording the frame number and potentiostat time throughout the experiment (Figure 1).
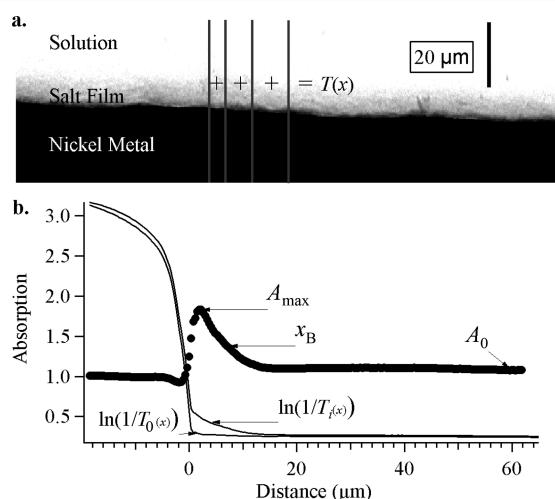

Figure 1. Illustration of how the raw radiograph images were converted to 1-D data. Part a is an example of a raw radiography image with vertical profile lines (gray lines) that contain the transmission as a function of distance. Part b shows how the $A(x)$ profile is obtained for each frame and illustrates the variables, maximum absorption (A_{max}), salt film boundary (x_B), and base level absorption (A_0) used in the Results and Analysis.

From the WAXS data, a simple estimate of the total volume of crystalline salt present (V_s) could be obtained by integration of the area under seven diffraction peaks (from patterns of the type shown in Figure 2) after subtraction of a straight line background interpolated from neighboring regions free of diffraction peaks. Errors in the observed salt volume were taken as the standard deviation of the volume calculated from each peak.

The 2-D SAXS images were converted to 1-D data using the Nika package available for Igor Pro[21] by integration over sectors spanning from 85° to 95° and 265° to 275°. The range of integration was chosen such that the intensity profile across the azimuthal angle, φ, did not significantly change; the minimum fwhm of $I(\varphi)$ vs φ within 0.05 Å^{-1} ≤ q ≤ 0.1 Å^{-1} in all four experiments was found to be ca. 10°. After image integration, 1-D plots of intensity versus the magnitude of the
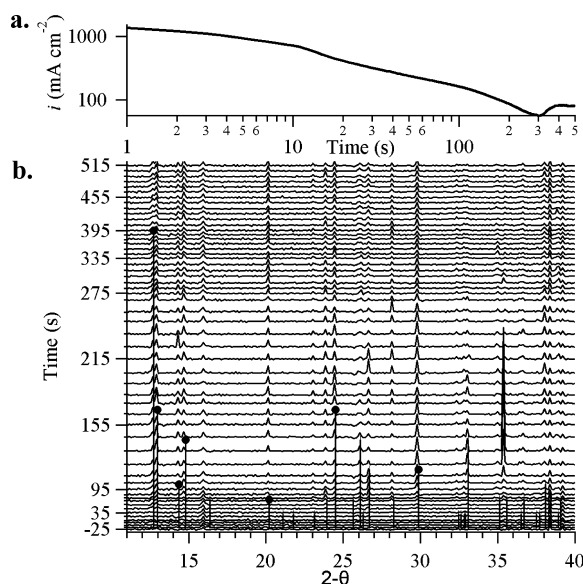
Figure 2. (a) Evolution of current with time following application of a potential step and (b) a stack plot of X-ray diffraction patterns obtained every 30 s. The time stamp of each diffraction pattern is shown to the left of the plot. Faint diffraction peaks from $NiCl_2(H_2O)_6$ can be observed at 60 s, followed by clear peaks at 90 s and is reproducible in potentiostatic experiments to 1.4 and 1.8 V. The seven strongest diffraction peaks chosen for total volume analysis are denoted by dots. The strong peak at $2\theta = 35.5°$ corresponds to nickel metal.

scattering vector, q, were obtained with q defined by the equation:

$$q = 4\pi\frac{\sin(\theta)}{\lambda} \tag{1}$$

where θ is half of the scattering angle, and λ is the wavelength of the X-ray beam.

Time Resolved Radiography. Fast radiography experiments were performed at the Swiss Light Source (SLS) on the TOMCAT Beamline at 15 keV. The 2-D images were obtained using pixel size of 0.37 μm by 0.37 μm and an imaged area of 760 μm (h) by 260 μm (v). The raw images were synchronized with the electrochemical data by using the same method mentioned in Section 2.a.

In order to calculate the transmission, T, from radiographs, the incident beam intensity profile (flat field) was measured with the sample removed from the beam and dark field measurements were made at the start and finish of every sequence of measurements. An average intensity profile of transmission versus vertical distance from the electrode surface $T(x)$ was obtained by addition of all vertical profiles in each image (Figure 2a). Because the interface is not perfectly horizontal, the vertical profiles were shifted to align them to a common reference point defined as the point of maximum derivative in each vertical transmission profile. This is an appropriate reference point since the X-ray absorption of nickel metal is an order of magnitude greater than the $NiCl_2(H_2O)_6$ salt, and therefore the reference point will be located within the metal and hence unaffected by the presence or absence of a salt film.

Quantitative interpretation of the transmission profiles requires accurate knowledge of the path length of X-rays in the solution. Unfortunately, this is not available due to the necessary presence of a layer of epoxy resin of unknown thickness used during cell construction and because of the possibility of some distortion of the Kapton windows. In order to take this into account, absorbance profiles, $A(x)$, were derived, which are considered proportional to the supersaturation of the solution and the presence of any salt by the Beer–Lambert Law. This was accomplished by normalization of each $A(x)$ profile to the absorbance profile taken from the saturation solution, obtained after all of the salt film was dissolved.

The plot of a typical $A_i(x)$ curve, 300 s after a potentiostatic step, is shown in Figure 2b. The absorption profile of frame i, $A_i(x)$ is defined by the equation:

$$A_i(x) = \frac{\ln(T_i(x))}{\ln(T_0(x))} \tag{2}$$

where T_i is the averaged transmission profile at frame i, and T_0 is the averaged transmission profile taken during a period when the potential is zero after a sufficient time had elapsed to ensure that all salt crystals had dissolved and to allow the concentration profile to level out to a value close to saturation (4.45 M for $NiCl_2(H_2O)_6$) in the 50 μm region of interest in this study. For a 1.5 mm deep pit, the profiles collected between 50 and 150 s after the step to 0 V (from 1.6 V) provides a suitable reference. It can be shown that the concentration of nickel chloride does not change by more than 0.3 M between 50 and 150 s for all data presented here. Errors arising from minor changes in $A(x)$ during this period propagate through the subsequent analysis. The value of A represents contributions from concentrations of Ni(II) and Cl species above saturation as well as any salt present, which is assumed to be $NiCl_2(H_2O)_6$.[9]

The $A(x)$ profile in Figure 2b can be described by three properties: the maximum absorption (A_{max}), the base level absorption far from the interface (A_0), and the salt film boundary (x_B). At steady state, A_0 is taken as the constant excess absorption far from the interface. The salt film boundary x_B is arbitrarily defined as the position having an absorption of 0.2 above the base level A_0, which corresponds to a $NiCl_2(H_2O)_6$ volume fraction of 0.09. Changes in A_{max} and x_B during a potentiostatic step experiment are reported here; only results from one of the potentiostatic steps to 1.6 V are shown for brevity. All results and trends obtained from the radiography experiments reported in this work are also observed in another step to 1.6 V and one to 1.0 V.

RESULTS AND ANALYSIS

Chronocoulometry and Wide-Angle X-ray Scattering. A typical potentiostatic step experiment is shown in Figure 2. Diffraction patterns were collected for a period of time at 0 V and at time, $t = 0$, the potential was stepped to 1.4 or 1.8 V. No diffraction peaks were observed at 0 V, but clear diffraction peaks were observed approximately 90 s after the potentiostatic step to either potential. The diffraction peaks correspond well to those of $NiCl_2(H_2O)_6$ as reported by Crook;[9,22] there are some differences between the expected and experimental positions but slight variation in the cell parameters for $NiCl_2(H_2O)_6$ is expected.[22-24] These experiments were performed twice to 1.4 V and twice to 1.8 V. All SAXS/XRD trends reported in this work were observed at both potentials.

The data show that the dominant crystalline phase is $NiCl_2.6H_2O$ and by close inspection of Figure 1 is can be seen

6726

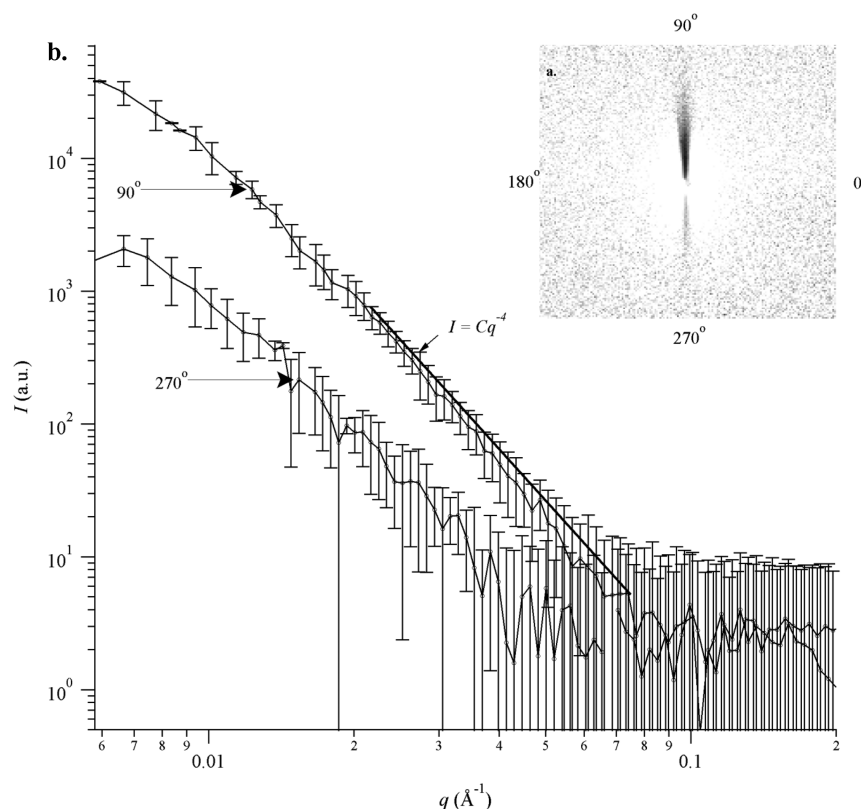dx.doi.org/10.1021/jp311666w | J. Phys. Chem. B 2013, 117, 6724–6732

Figure 3. (a) Typical SAXS image obtained 60 s after the potentiostatic step. (b) Log−log plot of typical anisotropic SAXS obtained from sector integration at 90° and 270° from the image shown in Figure 3a.

that amount of crystalline material increases from zero to some maximum value and then falls to a smaller constant value. This observation was quantified by calculation of the of the integrated diffraction intensities and is discussed in detail in with the results of the SAXS measurements.

Small Angle X-ray Scattering. The key and unexpected experimental finding of this study is that approximately 10 s after the change in potential, anisotropic small angle scattering is observed, which increases to a maximum at approximately 60 s. Figure 3a shows a raw SAXS image at 60 s showing a strong signal at 90° and 270°. Figure 3b shows the resulting 1-D SAXS data averaged over 10° sectors at 90° and 270° (corresponding to scattering vertically up and down, respectively). The shapes of the SAXS profiles are similar for both sectors, having power-law decays in intensity somewhat greater than q^{-4}. The shapes and temporal behavior of both of these scattering curves are essentially the same (apart from their magnitude) up to 120 s. Since the scattering signal at 270° is smaller than that at 90°, scattering must arise from an oriented anisotropic population near the interface (the signal at 270° being attenuated by passage through the nickel substrate). SAXS data obtained from the 10° sector at 90° are analyzed here because the signal-to-noise is lower at 270°. Furthermore, since scattering is never observed at the 0° and 180° sectors, we conclude that the source of scattering must have very large dimensions (>1 μm) parallel to the metal surface.

The presence of a q^{-4} scattering law, usually called Porod scattering, indicates the presence of a step change in scattering density within the system under study. This scattering is observed at large values of q and is the weak scattering (kinematic) limiting law for interface scattering. At smaller values of q, the scattering is stronger and assumptions of

kinematic scattering are no longer valid; such strong scattering must be analyzed by the theory of X-ray reflectivity. In this case, the magnitudes of scattering out and into the plane of the electrode surface are quite different. For a planar interface, the limits of reflectivity are respectively unity or zero for scattering away from or into the electrode surface: total external reflection or simple absorption.

SAXS/Reflectivity Modeling. The scattering that is observed in the early stage of dissolution arises from the interface between the electrode and the solution. Since this interface is present throughout the experiment, the importance of the observation of a SAXS signal lies in the anisotropy and magnitude of the scattering. Given the equivalence of reflectivity and Porod scattering in the weak scattering limit, the analytical tools developed for either the study of surface X-ray scattering or SAXS are both valid for analysis of these results. Here we choose to use the formalism of SAXS, since it is simpler and arguably more consistent with the method of data collection. These data were collected with a fixed sample position relative to the beam—whereas in reflectivity studies, the reflectivity is measured as a function of the incident angle. Furthermore analysis of these experiments in terms of X-ray reflectivity requires knowledge of the X-ray optical properties of the electrode and electrolyte including density and composition profiles.

Small angle scattering requires a difference in electron density between the scattering and matrix phase.[19] A power-law decay in q, greater than q^{-2}, and presence of only one possible Guinier knee (Figure 3b) indicate that only information about the smallest dimension of the layer is accessible. The other two dimensions (both parallel to the surface) are assumed to be too large for the observed q-range at 90°. To obtain the appropriate
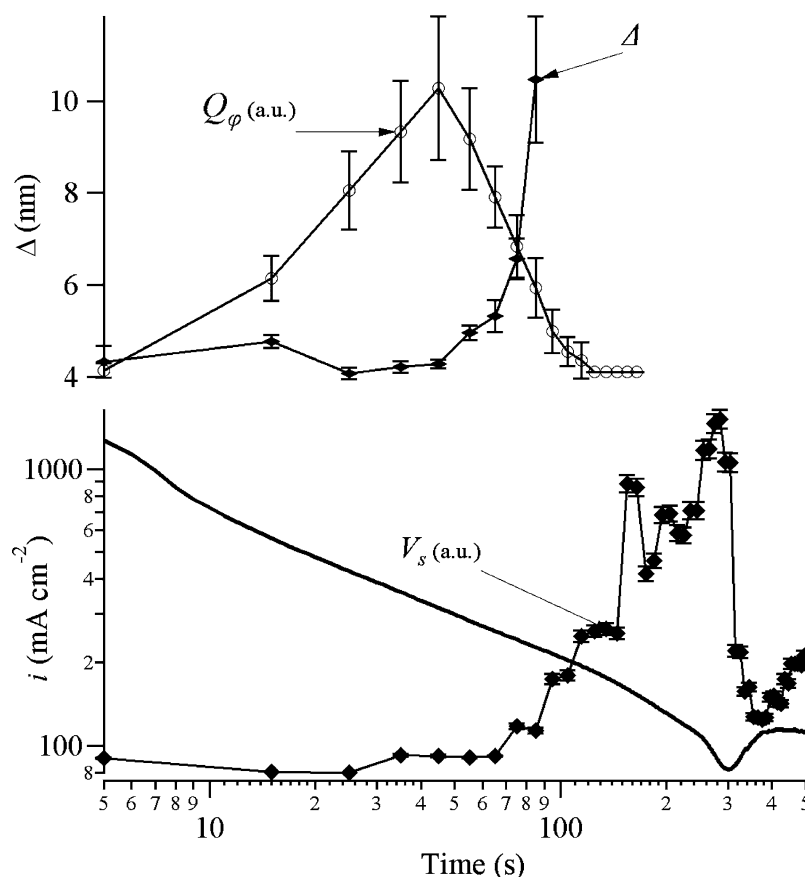
Figure 4. Plot of the total scattering (Q), salt volume (V_s), transition layer thickness (Δ), and current density (i), as a function of time for potentiostatic step from 0 to 1.4 V.

power-law decay in q from an anisotropic surface layer, possible orientations of the layer must be accounted for. The orientation of normals, perpendicular to the average electrode surface, can be described by two distribution functions, one along the direction of the beam, and the other the horizontal perpendicular to the beam. SAXS images (Figure 3a) indicate that the latter distribution is $\pm 5°$ (Section 2a). The distribution about the horizontal axis parallel to the beam direction can be estimated to be approximately $\pm 20°$ from the density profile of the electrode surface from the absorption profile through the Ni foil/solution interface and shown in Appendix A of the SI. For the range of q values (corresponding to scattering angles much less than $20°$) observed here, it is reasonable to assume a uniform distribution.

A q^{-4} scattering law arises from the presence of a sharp interface and to account for the observed decays, greater than q^{-4}, the presence of a smooth electron density gradient between the scattering and matrix phase must be invoked.[25] These smooth transitions can be accounted for by convoluting an ideal (step) electron density distribution with a smoothing function, assumed to be a Gaussian.[25,26] This convolution results in an electron density function that contains a transition layer between the scattering layer and adjacent solution, which would otherwise be zero in the ideal case. Therefore, an equation that takes into account the ideal intensity decay in q of q^{-4} and the nonideal transition layer thickness is fit to the high q-region (0.03 Å^{-1} < q < 0.075 Å^{-1}), which leads to a simple scattering model:

$$I(q) - [Fl] = \frac{K_2}{q^4}e^{(-\sigma^2 q^2)}$$
(3)

$$[Fl] = \frac{K_1}{q}$$
(4)

where, σ is the standard deviation of the Gaussian smoothing function, $[Fl]$ is the background, and K_1 and K_2 are constants;[25,26] the background term, $[Fl]$, is assumed to be constant. Equation 3 was fit to all of the data by first obtaining K_1 from the mean intensity values between, 0.08 Å^{-1} < q < 0.2 Å^{-1}. The values of K_2 and σ were then varied to fit eq 3 to the background-subtracted intensity by a least-squares method. Because the model transition layer is actually a sigmoid function, the fwhm of the Gaussian smoothing function is used to represent the transition layer thickness, Δ and is calculated from σ by the standard equation:

$$\Delta = 2\sqrt{2\ln(2)}\sigma$$
(5)

Scattering Layer Evolution. While the exact structure of the interfacial phase which gives rise to the anisotropic scattering is not certain, it is possible to determine the relative amount of the phase present by calculation of a suitable invariant.[19] Since the scattering is anisotropic, a pseudoinvariant, Q_φ, has been chosen to represent the total scattering, and calculated by the equation:
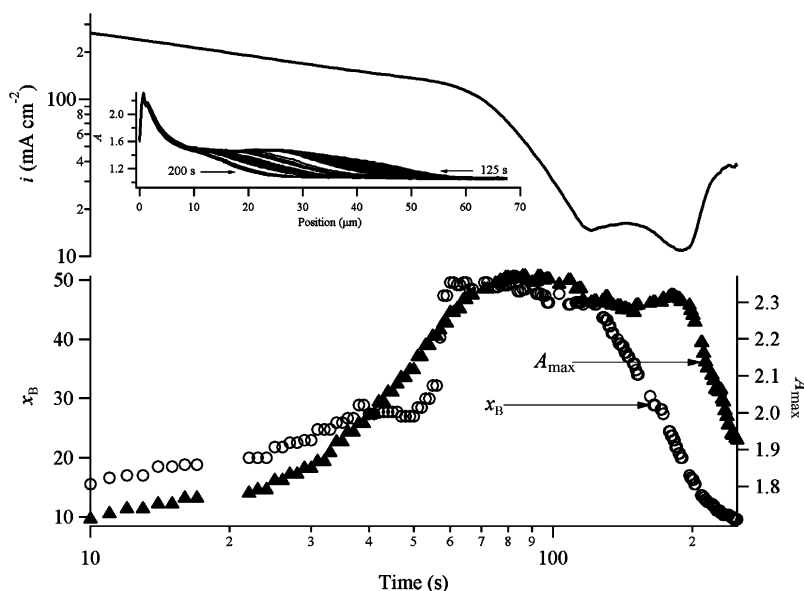
Figure 5. Plot of A_{max}, x_B, and current density as a function of time for a potential step experiment to 1.6 V. The inset plot shows that the value of A between 10 μm and x_B stays approximately constant at 1.45 ± 0.5 during salt dissolution.

$$Q_\varphi = \int_{0.006}^{0.2} \int_{85}^{95} I(q)q^2 \, d\varphi dq$$

$$\cong \frac{\pi}{18} \int_{0.005}^{0.05} I(q)q^2 \, dq$$

$$\propto \overline{\Delta\eta^2} V \tag{6}$$

where q is the magnitude of the scattering vector, I is the averaged intensity over the 10° span, V is the volume of the surface layer and $\overline{\Delta\eta^2}$ is the contrast; integration limits are set to the available q-range. Equation 6 is used as the best available equation for the total scattering of the anisotropic scattering population. It can be seen that the total scattering is proportional to the total scattering volume and contrast, which are physically meaningful parameters.

The time-dependence of the SAXS total scattering (Q_φ), crystalline salt volume (V_s), transition layer thickness (Δ) and the current density (i), following the application of a potentiostatic step to 1.4 V is shown in Figure 4. It can be seen that Q_φ increases to a maximum at ca. 60 s, at which time the surface layer has a small transition layer thickness, Δ, (sharp interface) and is fully developed. Before the maximum Δ is reached, the value of Q_φ increases by a factor of 3, with little change in the scattering shape within experimental error. Only after the peak in Q_φ does Δ increase monotonically. Therefore, values of delta cannot be an artifact of a weaker SAXS signal, which was also observed before the peak in Q_φ. Values of Δ and salt volume (V_s) always increase rapidly after Q_φ reaches a maximum, showing a strong correlation between the three parameters. The same pattern of behavior was seen in all experiments that consisted of potentiostatic steps to −1.4 V and −1.8 V.

Radiography Results. Figure 5 shows how A_{max} and x_B evolve as a function of time after a potentiostatic step to 1.6 V. Just after the step, A_{max} increases rapidly, while the current is decreasing as the concentration of dissolved nickel increases near the interface. The salt film boundary, x_B, and the maximum absorbance A_{max} increase during the first 60 s as supersaturation extends far from the interface. The X-ray absorbing salt layer

then forms but the current and supply of Ni(II) is now too low to keep pace with diffusion of nickel from the salt layer into the solution which, results in thinning of the in salt layer.[8] During dissolution, x_B decreases before the current minimum, following the similar trend in V_s shown in Figure 4. The inset in Figure 5 shows the general trend of the profile, $A(x)$, as the salt dissolves toward the interface. The value of A between ca. 8 μm and x_B has a maximum value of 1.45 ± 0.5 and remains constant during salt film dissolution.

■ DISCUSSION

The events which follow the imposition of a potential step may be divided into three time periods during which there is one dominant phenomenon present. These are formation of an oriented interface, nucleation, and dissolution to steady state, illustrated by the sequence of radiographs shown in Figure 6. Before the potentiostatic step, the Ni foil is at 0 V, and the concentration of the solution adjacent to the interface will be near to saturation. The gray scale for Figure 6 has been set such that solutions whose concentration is near saturation are denoted by white in the image. The discussion below will be grouped around the three stages identified above.

Formation of an Oriented Interface. Shortly after the imposition of a potentiostatic step (step 2 in Figure 6), an anisotropic SAXS signal is observed (Figure 3) caused by scattering from the electrode−electrolyte interface. Continued Ni metal dissolution results in local increases in the concentration of Ni(II), along with the formation of a transient boundary (Figure 4) where the electron density transitions from that of the scattering layer to the adjacent solution. Before the potential step is applied to initiate dissolution, no interfacial scattering is visible because the interface is rough on a microscopic length scale. Interface scattering will surely exist but since the local surface scattering vectors will be uniformly distributed around the direct beam, the scattering will be too weak to observe. However, under conditions of rapid dissolution, the high electric fields present in the vicinity of asperities cause preferential dissolution of asperities and smoothing of the electrode surface. This smoothing leads the
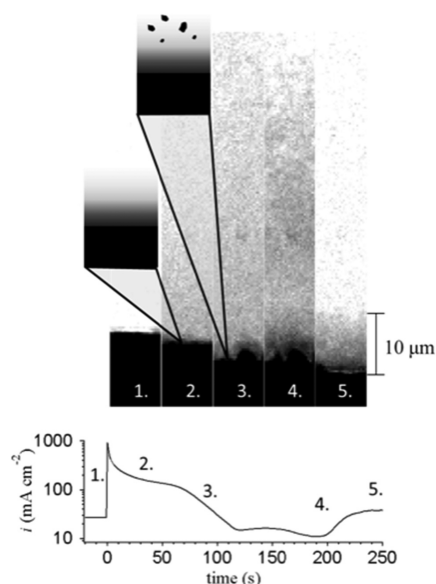
Figure 6. Time series of radiographic images for a small section of the electrode, before, during, and after the imposition of a potential step to 1.4 V. A schematic interpretation of the radiographic images is given below each radiograph. The times corresponding to the radiographs are indicated in Figure 4.

interface scattering to be directed in a common direction perpendicular to the surface and hence to become visible.

Continued dissolution and build up of dissolved Ni(II) near the interface results in a well-defined smooth surface layer at ~60 s and shown in step two in Figure 6. As time progresses, the value of Q_φ increases as asperities dissolve, and more of the interface scattering becomes directed into the vertical plane. We also note that increases in Q_φ can be equally attributed to a change in volume or contrast of the adjacent layer (eq 6).

Nucleation. Following the formation of the smooth interfacial layer, nucleation of crystalline $NiCl_2(H_2O)_6$ occurs inside the region of supersaturated nickel chloride solution. As shown in Figure 5, the total salt volume (V_s) rapidly increases only after the smooth interfacial layer is fully developed. Crystal nucleation theory predicts rapid nucleation rates when a critical supersaturation value is reached, regardless of the crystal structure.[27] Critical supersaturation ratios predicted by the method of Ruckenstein depend on the value of the monomer–monomer and monomer–solvent interaction, which also depends on the crystal structure.[28] It is hypothesized that a critical concentration of Ni(II) is reached, and nucleation spontaneously occurs at or near the surface layer. Typical supersaturation ratios for crystal nucleation vary significantly between 2 to 300, with the predicted ratio of molten salt to saturated nickel chloride at 15. Although it is not clear where the crystal nucleation occurs, it is likely to take place at the boundary where more water is available. Once nucleated, crystallites are transported away from the surface layer by diffusion or diffusion/electrophoresis, depending on whether or not the particles are charged. This process is shown schematically as Step 3 in Figure 6.

During crystal nucleation and growth, scattering from the surface begins to disappear (Figure 4) and the transition layer thickness increases. An increase in the transition layer thickness suggests that the surface layer boundary transitions to a continuous gradient, too large to give a SAXS signal. An alternative explanation is offered by the presence of increasing surface roughness. Thus, continued nucleation and growth causes the concentration of nickel in the surface layer to decrease. Without a well-defined surface or sufficient contrast, the SAXS signal completely disappears by ~120 s.

Interestingly, the current density begins a rapid decrease shortly after the interface scattering disappears, Substantial surface roughness is also observed in the radiographs, indicating that the dissolution kinetics across the surface vary; this is not the case during times where the interface scattering can be observed. The disappearance of the interface scattering and appearance of a crystalline salt layer is thus considered to substantially change the dissolution kinetics at the metal surface. Variations in the surface dissolution rate are very likely a consequence of the salt film presence, which comprises a loose ensemble of salt crystals and where current can only flow through electrolyte-filled gaps between crystals. Thus, a crystal containing salt film will reduce the overall rate of dissolution and make dissolution intrinsically inhomogeneous.

Dissolution to Steady State. Crystal nucleation and growth continues after the disappearance of the interface scattering until the salt film is too thick. At this point, both the salt film boundary, x_B, (Figure 5) and the salt volume (Figure 4) reach a maximum value and begin to decrease at an inflection point before the current minimum. This is shown in step 4 of Figure 6. Agreement between the XRD and radiography data leads us to conclude that salt crystals extend far out into solution (>20 μm) before they begin to dissolve. Strong correlation between salt dissolution and a change in the current density is likely to be due to sudden changes in the resistance between the working and reference electrode; although the ion flux away from the reaction plane is also expected to increase as more salt film dissolves.

During dissolution, A remains constant at 1.45 ± 0.5 between ca. 8 μm and x_B, suggesting that ion transport within this region is restricted enough to prevent homogeneous dissolution inside but fast enough at the boundary to cause the salt film to dissolve. The volume fraction of salt at $A = 1.45$ can be calculated, with few assumptions. Between 8 μm and x_B, salt is not dissolving or growing, as the concentration must be near saturation. Using the appropriate values of μ/ρ for Ni, Cl, H, and O (at 15 keV), the density of saturated $NiCl_2(H_2O)_6$ (1.42 g cm^{-3} at 4.45 M) and the density of $NiCl_2(H_2O)_6$ (1.92 g cm^{-3}), the volume fraction of salt (ν_{salt}) is calculated to be 0.2. Although no volume fraction of salt has been reported in nickel salt films, the porosity has; the porosity is defined as the area available for transport divided by the actual geometrical area. To a first approximation, salt volume fraction and porosity are related by the following: porosity ≈ $1 - \nu_{salt}$. The calculated porosity in the salt film during this time is much larger than the steady state values of ca. 0.1% reported by others.[8,11] This large discrepancy is not surprising since the previous work considered the steady state film rather than the transient one observed here. In addition, previous calculations have assumed that all of the resistance is due to the presence of salt.

Finally, the salt film reaches a steady state thickness and shown as the final step in Figure 6. Consequently, the current also reaches steady state. The time required to reach a steady state current ultimately depends on how fast the system can progress through the above-mentioned steps. In particular, salt film dissolution (step 4 in Figure 6) to steady state would depend strongly on the ion transport out of the pit.

CONCLUSIONS

In this work, we provide experimental evidence for interfacial and near-interfacial phenomena when instantaneous high dissolution conditions are imposed on a restricted transport system. Following a potentiostatic step, a highly supersaturated layer of salt solution is formed. In the presence of a highly supersaturated solution next to the interface, the SAXS signal indicates that the surface morphology becomes smooth. When a critical supersaturation ratio is reached, nucleation of salt crystals occurs in or near the surface layer. Nucleation of salt crystals leads to surface roughening and a sharp decrease in the current density. This indicates that the microscopic heterogeneity inherent with the formation of a crystalline salt layer leads inevitably to surface roughening. In the past, the presence of salt films has been invoked to explain the process of electropolishing. However, our work shows that the presence of *crystalline* material adjacent to the dissolving electrode is detrimental to the production of a smooth electrode surface as evidenced by our small angle scattering data.

Analysis of XRD and radiography data lead us to conclude that a temporarily thick salt film forms and dissolves toward the metal surface to a steady state thickness. During dissolution, ion transport between ca. 8 μm and the salt film boundary is restricted enough to prevent homogeneous dissolution of the salt film. A salt volume fraction of ca. 20% is calculated from within the dissolving salt film, which is much lower than that that previously found for steady state salt films.

ASSOCIATED CONTENT

Supporting Information

A description of the scattering geometry and derivation of the SAXS analysis (Appendix A). This material is available free of charge via the Internet at http://pubs.acs.org.

AUTHOR INFORMATION

Corresponding Author

*Phone: +441235778984; e-mail: trevor.rayment@diamond.ac.uk.

Notes

The authors declare no competing financial interest.

ACKNOWLEDGMENTS

REFERENCES

(1) El Aal, E. E. A.; Zakria, W.; Diab, A.; El Haleem, S. M. A. Anodic Dissolution of Nickel in Acidic Chloride Solutions. *J. Mater. Eng. Perform.* **2003**, *12*, 172−178.

(2) Beck, T. R.; Alkire, R. C. Occurrence of Salt Films During Initiation and Growth of Corrosion Pits. *J. Electrochem. Soc.* **1979**, *126*, 1662−1666.

(3) Laycock, N. J.; Newman, R. C. Localised Dissolution Kinetics, Salt Films and Pitting Potentials. *Corros. Sci.* **1997**, *39*, 1771−1790.

(4) Hunkeler, F.; Krolikowski, A.; Bohni, H. A Study Of The Solid Salt Film On Nickel And Stainless-Steel. *Electrochim. Acta* **1987**, *32*, 615−620.

(5) Landolt, D.; Chauvy, P. F.; Zinger, O. Electrochemical Micromachining, Polishing and Surface Structuring of Metals: Fundamental Aspects and New Developments. *Electrochim. Acta* **2003**, *48*, 3185−3201.

(6) Grimm, R. D.; Landolt, D. Salt Films Formed During Mass-Transport Controlled Dissolution Of Iron-Chromium Alloys In Concentrated Chloride Media. *Corros. Sci.* **1994**, *36*, 1847−1868.

(7) Grimm, R. D.; West, A. C.; Landolt, D. Ac Impedance Study Of Anodically Formed Salt Films On Iron In Chloride Solution. *J. Electrochem. Soc.* **1992**, *139*, 1622−1629.

(8) Danielson, M. J. Transport-Properties of Salt Films on Nickel in 0.5N HCl. *J. Electrochem. Soc.* **1988**, *135*, 1326−1332.

(9) Rayment, T.; Davenport, A. J.; Dent, A. J.; Tinnes, J. P.; Wiltshire, R. J. K.; Martin, C.; Clark, G.; Quinn, P.; Mosselmans, J. F. W. Characterisation of Salt Films on Dissolving Metal Surfaces in Artificial Corrosion Pits via in Situ Synchrotron X-ray Diffraction. *Electrochem. Commun.* **2008**, *10*, 855−858.

(10) Sridhar, N.; Dunn, D. S. In Situ Study of Salt Film Stability in Simulated Pits of Nickel by Raman and Electrochemical Impedance Spectroscopies. *J. Electrochem. Soc.* **1997**, *144*, 4243−4253.

(11) West, A. C.; Grimm, R. D.; Landolt, D.; Deslouis, C.; Tribollet, B. Electrohydrodynamic Impedance Study of Anodically Formed Salt Films on Iron in Chloride Solutions. *J. Electroanal. Chem.* **1992**, *330*, 693−706.

(12) Laycock, N. J.; Noh, J. S.; White, S. P.; Krouse, D. P. Computer Simulation of Pitting Potential Measurements. *Corros. Sci.* **2005**, *47*, 3140−3177.

(13) West, A. C. Comparison of Modeling Approaches for a Porous Salt Film. *J. Electrochem. Soc.* **1993**, *140*, 403−408.

(14) Newman, J. S.; Thomas-Alyea, K. E. *Electrochemical Systems*, 3rd ed.; John Wiley: Hoboken, NJ, 2004; pp xx, 647.

(15) Varela, L. M.; Carrete, J.; Garcia, M.; Gallego, L. J.; Turmine, M.; Rilo, E.; Cabeza, O. Pseudolattice Theory of Charge Transport in Ionic Solutions: Corresponding States Law for the Electric Conductivity. *Fluid Phase Equilib.* **2010**, *298*, 280−286.

(16) Dufreche, J. F.; Bernard, O.; Turq, P. Transport Equations for Concentrated Electrolyte Solutions: Reference Frame, Mutual Diffusion. *J. Chem. Phys.* **2002**, *116*, 2085−2097.

(17) Van Damme, S.; Deconinck, J. Relaxation Effect on the Onsager Coefficients of Mixed Strong Electrolytes in the Mean Spherical Approximation. *J. Phys. Chem. B* **2007**, *111*, 5308−5315.

(18) Luo, J. L.; Hileman, O. E.; Ives, M. B. Salt Film Development During Pitting of Nickel. *Corros. Sci.* **1993**, *35*, 73−81.

(19) Glatter, O.; Kratky, O. *Small Angle X-Ray Scattering*; Academic Press: New York, 1982.

(20) Berry, A.; Helsby, W. I.; Parker, B. T.; Hall, C. J.; Buksh, P. A.; Hill, A.; Clague, N.; Hillon, M.; Corbett, G.; Clifford, P.; et al. The Rapid2 X-ray detection system. *Nucl. Instrum. Methods Phys. Res. A* **2003**, *513*, 260−263.

(21) Ilavsky, J.; Jemian, P. R. Irena: Tool Suite for Modeling and Analysis of Small-Angle Scattering. *J. Appl. Crystallogr.* **2009**, *42*, 347−353.

(22) Crook, W. W.; Jambor, J. L. Nickelbischofite, a New Nickel Chloride Hydrate. *Can. Mineral.* **1979**, *17*, 107−109.

(23) Kleinberg, R. Crystal Structure of $NiCl_2 \cdot 6H_2O$ at Room Temperature and 4.2 K by Neutron Diffraction. *J. Chem. Phys.* **1969**, *50*, 4690−4696.

(24) Mizuno, J. Crystal Structure of Nickel Chloride Hexahydrate, $NiCl_2 \cdot 6H_2O$. *J. Phys. Soc. Jpn.* **1961**, *16*, 1574−&.

(25) Ruland, W. Small-Angle Scattering of 2-Phase Systems—Determination and Significance of Systematic Deviations from Porods Law. *J. Appl. Crystallogr.* **1971**, *4*, 70−.

(26) Kim, M. H. Modified Porod's Law Estimate of the Transition-Layer Thickness between Two Phases: Test of Triangular Smoothing Function. *J. Appl. Crystallogr.* **2004**, *37*, 643−651.

(27) Ruckenstein, E.; Djikaev, Y. S. Recent Developments in the Kinetic Theory of Nucleation. *Adv. Colloid Interface Sci.* **2005**, *118*, 51−72.

(28) Narsimhan, G.; Ruckenstein, E. A New Approach for the Prediction of the Rate of Nucleation in Liquids. *J. Colloid Interface Sci.* **1989**, *128*, 549−565.

6732

dx.doi.org/10.1021/jp311666w | *J. Phys. Chem. B* 2013, 117, 6724−6732